Chemical Engineering Journal 504 (2025) 158784

Contents lists available at ScienceDirect

Chemical Engineering Journal

journal homepage: www.elsevier.com/locate/cej

4D printed mortise-tenon mechanical-electromagnetic multifunctional pixel metamaterials

Xiaozhou Xin [a], Chunli Yang [b], Zhicheng Wang [a], Yin Xing [a], Chengjun Zeng [a], Liwu Liu [a,*], Yanju Liu [a,*], Jinsong Leng [b]

[a] Department of Astronautical Science and Mechanics, Harbin Institute of Technology (HIT), P.O. Box 301, No. 92 West Dazhi Street, Harbin 150001, People's Republic of China

[b] Center for Composite Materials and Structures, Harbin Institute of Technology (HIT), No.2 Yikuang Street, P.O. Box 3011, Harbin 150080, People's Republic of China

ARTICLE INFO

Keywords:
4D printing
Shape memory polymers
Metamaterials
Mortise-tenon structures
Composite aerogel

ABSTRACT

Mechanical metamaterials are complicated artificial materials composed of periodically interconnected microstructures, exhibiting extraordinary mechanical properties not available in natural materials. However, the periodically interconnected design model results in most current metamaterials suffering from following limitations: *i*) lack of modularity and repairability, *ii*) damage transmittability, *iii*) weak scalable fabrication and limited fabrication dimensions, and *iv*) single functionality. Inspired by the connection mechanism of mortise-tenon structures and the configuration of brick–mortar structures, 4D printed mortise-tenon mechanical-electromagnetic multifunctional pixel metamaterials (MPMs) are developed in this work. The innovative binding constraint, derived from the Hanfu silk ribbon, has been proposed, achieving reliable connection of the MPM while suppressing damage transmission. The modular structure design strategy of the PMM enables large-scale and scalable manufacturing, while also achieving repairability. The developed mechanical-electromagnetic MPMs have multifunctional properties, including lightweight, energy absorption, electromagnetic wave absorption (RL_{min} –32.84 dB) and reconfigurability, which have a wide range of application prospects in the field of electromagnetic stealth equipment.

1. Introduction

Mechanical metamaterials are complicated artificial materials composed of rationally designed periodic arrangements cells, exhibiting mechanical properties not found in natural materials.[1–7] The diverse configurations and highly customisable performance of mechanical metamaterials creat opportunities for designing macroscopic physical properties, contributing to the development of advanced functional devices.[8–12] The evolution of metamaterials is toward programmability, high designability and multifunctionality with the widespread application of metamaterials in aerospace, flexible electronics, etc.

However, the properties of mechanical metamaterials depend on the configuration of the microstructures, meaning that the geometrical parameters and mechanical properties of the fabricated metamaterials are fixed, resulting in the lack of adaptability and reconfigurability.[13,14] The periodic interconnection design pattern facilitates the propagation of damage among cells, leading to the rapid expansion of damage.[15,16] Meanwhile, the periodic interconnect design model limits the large-scale, scalable fabrication, modularity, and repairability of metamaterials. The scale of metamaterials is constrained by the dimension of the fabrication platform, which is difficult to realize large-scale fabrication. When the damage occurred in the cells of the metamaterial, the periodic interconnection model leads to the failure of the whole metamaterial and lack of repairability. More importantly, the research on metamaterials is mostly devoted to exploring the innovative design of configurations to broaden the extraordinary mechanical properties, while neglecting the development of structural–functional integrated metamaterials (such as mechanical and electromagnetic).

Shape memory polymer (SMP), a typical type of stimulus-responsive materials, can recover from the temporary configuration to its original configuration under external stimulus (thermal, magnetic, electrical, etc.), exhibiting variable stiffness, active deformation, etc. [17–23] 4D printing combined 3D printing technology with SMP, where the performance/functionality of the printed object can adaptively change over time. 4D printing mechanical metamaterials combine fine structural design with stimulus-responsive materials to enable the alteration of its

* Corresponding authors.
E-mail addresses: liulw@hit.edu.cn (L. Liu), yj_liu@hit.edu.cn (Y. Liu).

https://doi.org/10.1016/j.cej.2024.158784
Received 22 October 2024; Received in revised form 10 December 2024; Accepted 18 December 2024
Available online 21 December 2024

configuration/performance in response to external stimuli.[24–28] 4D printing endows metamaterials with programmability and reconfigurability in terms of configuration and mechanical properties, increasing the design freedom of metamaterials.[29–33] The typical pixel metamaterials consist of uncoupled constrained mechanical pixels and additional structures to fix the mechanical pixels (frames, etc.).[15,16,34] The independent mechanical pixels effectively prevents damage transmission while endowing the pixel metamaterials with modularity and repairability. However, the mechanical pixels in typical pixel metamaterials carry loads independently and cannot transfer loads to each other. The additional structure only maintains the configuration without involved in the deformation, which undoubtedly increased the weight of the metamaterial.

The most current mechanical metamaterials suffer from following limitations: *i*) the lack of modularity and repairability, *ii*) damage transmittability, *iii*) weak scalable fabrication capability and limited fabrication dimensions, and *iv*) single functionality. Here, 4D printed mortise-tenon mechanical-electromagnetic multifunctional pixel metamaterials (MPMs) consisting of multifunctional pixels (MPs) with brick–mortar structure were developed, which realized the integration of load-bearing, lightweight and electromagnetic wave (EMW) absorption capacity. Inspired by the silk ribbon of Hanfu (Chinese traditional dress), the binding constraint method between MPs were innovatively proposed to transfer loads between MPs without increasing the weight of metamaterials. The universality of the mortise-tenon design model was verified by employing typical additive manufacturing processes and printing filament. It was necessary to select the materials and cell types of metamaterials according to the usage requirements in practical applications. The MPM broke through the dimensional limitations of the fabrication platform, and enabled large-scale, modular, repairable, and scalable manufacture of metamaterials. The application prospects of mechanical-electromagnetic MPM in energy absorbing devices and electromagnetic stealth equipment were verified.

2. Results and discussion

2.1. Design of mechanical-electromagnetic MPM

Chinese architecture are constructed via mortise-tenon structures, connecting the discrete parts into the large-scale structure (Fig. 1A). Inspired by the connection mechanisms of mortise-tenon structures, the mortise-tenon mechanical-electromagnetic MPM with modularity, scalable manufacturing and repairability were designed (Fig. 1B1). The designed mechanical-electromagnetic MPM consisted of MPs with the brick–mortar structure arrayed (m, n) along the (x, z) axis, respectively (Fig. 1B1 and Fig. 1B2). In the construction of brick–mortar structures with cement mortar, the cement mortar was uniformly spread, and then the bricks were placed on top of the mortar to provide the robust connection of the brick–mortar structure (Fig. 1C). The developed MPs consisted of n_p multifunctional mortise-tenon metamaterials connected in series with modularization ability (Fig. 1B2). The multifunctional mortise-tenon metamaterials were constructed using mortise-tenon metamaterials and multistage ordered transition metal carbides/nitrides $Ti_3C_2T_x$@graphene oxide (MXene@GO) composite aerogel as "brick" and "mortar", respectively (Fig. 1B2 and Fig. 1D). MXene exhibits the characteristics of large specific surface area, high electrical conductivity, abundant surface functional groups, and lightweight.[35,36] The efficient absorptivity of MXene for the EMW was mainly attributed to its high specific surface area, efficient dielectric loss of the multipolarization mechanism, and the interfacial loss of the unique nanostructures. More importantly, MXene with 3D porosity is the lightweight and efficient absorber due to the abundant porosity, which not only contributes to the improvement of impedance matching, but also reduces the density, making it more favorable for EMW absorption.[37–41].

The mortise-tenon metamaterials ($L_x \times L_y \times L_z$) consisted of 12 independents, interlocking discrete connecting parts (Part 1 to Part 12), as shown in Fig. 1D2 and Movie S1. Among the 12 parts of the mortise-tenon metamaterials, Part 1 and Part 2, Part 3 and Part 4, Part 5 and Part 6, Part 7 and Part 8 had the same configuration. Part 1 and Part 2 were the main parts, Part 3 ~ Part 12 were the connecting parts. The parts were mortise and tenon jointed with each other through the concave-convex configuration to form the whole structure (Fig. 1D and Fig. S1). The mortise-tenon metamaterials integrated irregular discrete parts into the cube/rectangular/complex configuration by interlocking and mortising the discrete parts, which can maintain its configuration and exhibit macroscopic constitutive behavior under external loads (Fig. S1).

Scalable connecting mortise-tenon parts for interconnecting mortise-tenon metamaterials were constructed by arraying specific parts to make reliable, stable connections of the developed MP without redundant materials/structures. Fig. 1B and Movie S2 exhibit the CAD model and assembly process of MP ($n_p = 3$) by connecting mortise-tenon metamaterials via mortise-tenon connecting parts, respectively. Table S1 shows the CAD model for the connecting parts between mortise-tenon metamaterials. The mortise and tenon configuration characteristics endowed the integrated MP with modularity and repairability, and the configuration and arrangement of each mortise-tenon metamaterials in the MP were enabled to be designed according to the requirements. The designed MPs were uninterconnected discrete structures, and the additional structures such as frames were used to fix the MPs in the most researches, which prevented the MPs from transferring loads to each other and increased the weight of the metamaterial. Hanfu, traditional Chinese clothing, which is constrained the wide clothes by silk ribbons to maintain convenient movement of wearer (Fig. 1E). Inspired by the binding method of silk ribbon, the ribbon type binding method of MPM was proposed to ensure the load transfer and restrain the damage transfer between MPs, which further improved the modularity and maintainability of metamaterials without increasing the weight.

The lightweighting of multifunctional metamaterials was realised by introducing Octet(Fig. 1F1), Kelvin (Fig. 1F2), 3D Re-entrant (Fig. 1F3), and 3D chiral (Fig. 1F4) lattice metamaterial cells into each mortise-tenon parts (Fig. 1F). Table S1 shows the CAD models of the mortise-tenon connecting parts and the corresponding names based on the Octet cells. The parts of the mortise-tenon metamaterial were assembled according to the process shown in Movie S1. The geometric parameters, L_{xi}, L_{yi}, L_{zi}, d_i, R_c, t_c, were controlled the configuration and mechanical properties of the mechanical metamaterial cells (Fig. 1F). L_{xi}, L_{yi}, L_{zi} represented the lengths of the cells in the x ,y, and z directions, respectively. d_i represented the ligament diameters of the i-type cells ($i = l, k, r, c$). l, k, r, and c represented Octet, Kelvin, 3D Re-entrant, and 3D chiral lattice metamaterial cells, respectively. R_c, and t_c represented the circular radius and thickness of 3D chiral lattice metamaterial cells, respectively. The mortise-tenon metamaterials ($L_x \times L_y \times L_z = 73$ mm $\times$ 73 mm $\times$ 70 mm) were obtained by assembling each mortise-tenon parts consisting of metamaterial cells. Fig. 1G ~ 1I exhibit the CAD models of multifunctional pixel metamaterials, multifunctional pixels and multifunctional mortise-tenon metamaterials composed of lightweight cells. Fig. 1J exhibit the CAD models of the developed Octet(Fig. 1J1), Kelvin (Fig. 1J2), 3D Re-entrant(Fig. 1J3), and 3D chiral (Fig. 1J4) mortise-tenon metamaterials.

2.2. Modular and scalable fabrication of mechanical-electromagnetic MPM

The mortise-tenon metamaterials were fabricated by assembling the mortise-tenon parts (Fig. 2A), and the integration state was highly dependent on the fabrication accuracy. For example, the poor accuracy might result in fabricated mortise-tenon parts outside of the design dimensions, leading to the integrated metamaterial interference fit and initial assembly stresses. If the fabricated mortise-tenon parts were less than the design dimensions, the connection strength and stability of the

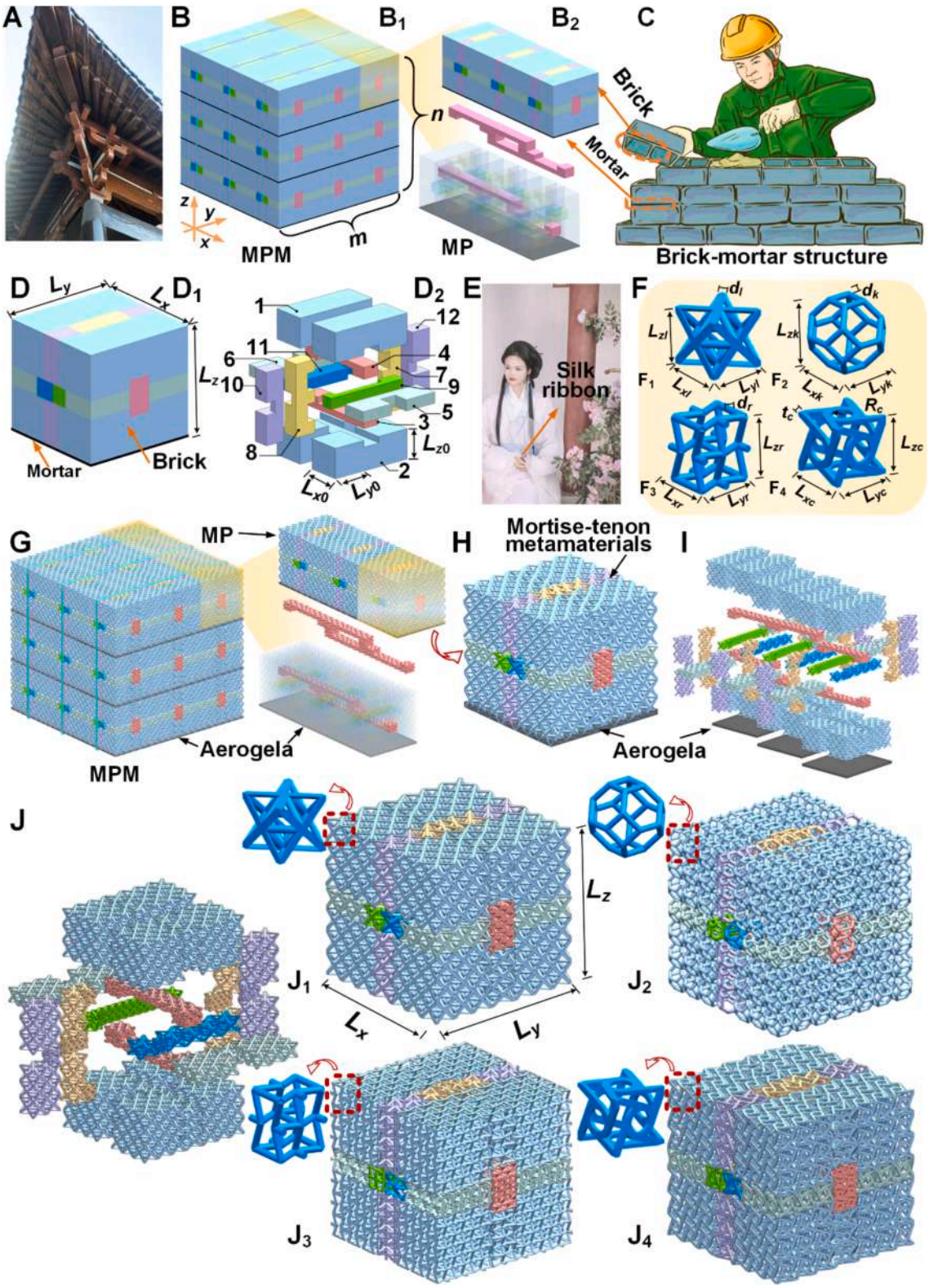

Fig. 1. (A) The mortise-tenon structures of Chinese architectures. (B) The CAD models of mortise-tenon type mechanical-electromagnetic MPM: (B_1) MPM; (B_2) MP. (C) The brick–mortar structure. (D) The multifunctional mortise-tenon metamaterials: (D_1) assembly view; (D_2) exploded view of mortise-tenon metamaterials. (E) The silk ribbons of Hanfu. (F) The lightweight metamaterial cells: (F_1)Octet, (F_2)Kelvin, (F_3)3D Re-entrant, and (F_4)3D chiral. (G) The mechanical-electromagnetic MPM composed of lightweight metamaterial cells. (H) Multifunctional mortise-tenon metamaterials and (I) exploded view of the MP. (J) The CAD models of mortise-tenon metamaterials consisting of different lightweight cells: (J_1) Octet; (J_2) Kelvin; (J_3) 3D Re-entrant; (J_4) 3D chiral.

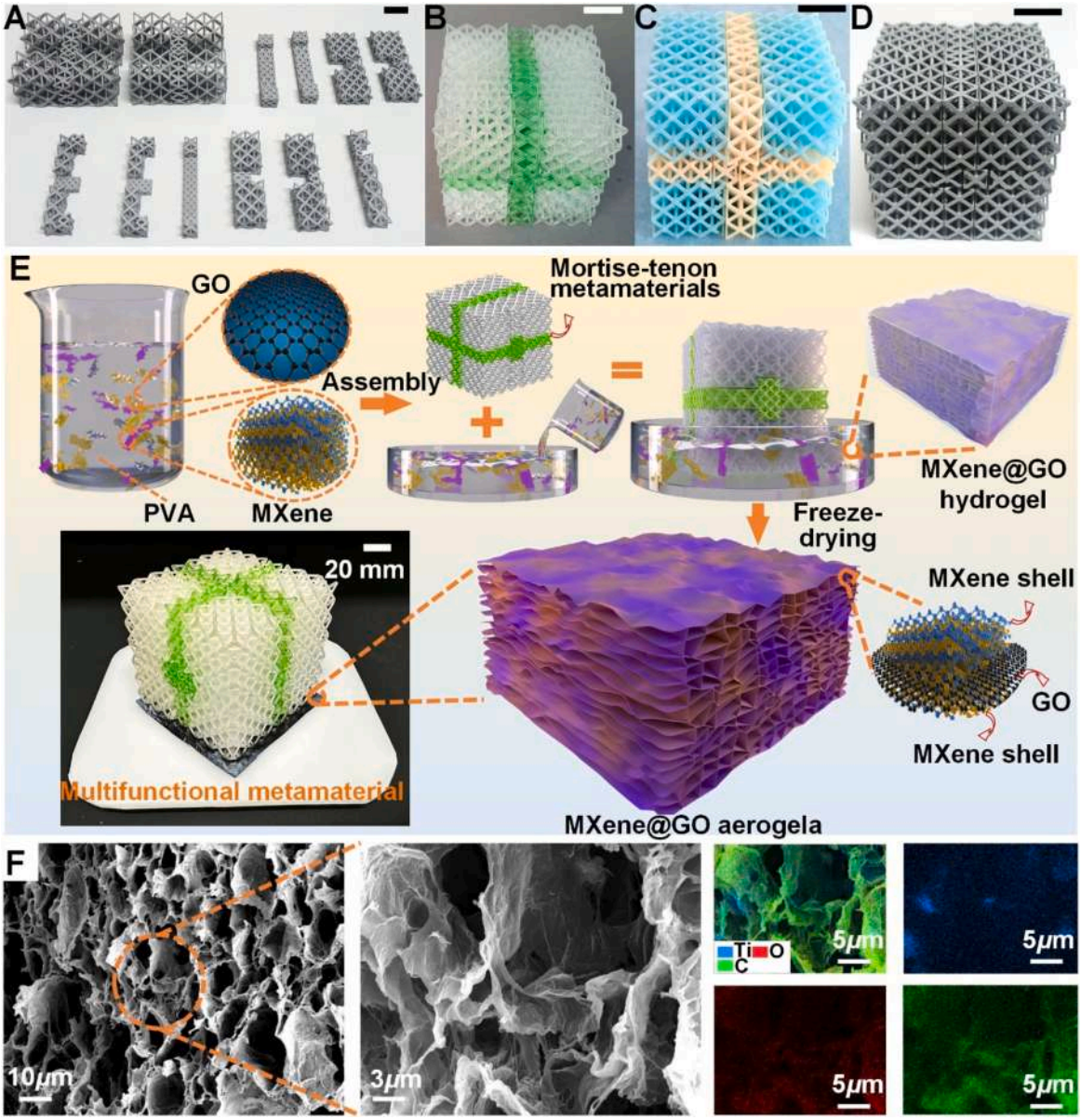

Fig. 2. The fabricated Octet mortise-tenon metamaterials: (A) the mortise and tenon parts. Mortise-tenon metamaterials fabricated by (B) rigid-SMP, (C) PLA-SMP and (D) aluminum alloys. The scale bar is 20 mm. (E) The fabrication process of the multifunctional metamaterials with brick–mortar structure. (F) The SEM and EDS scanning results of the mortar (MXene@GO composite aerogel).

metamaterial were affected. The components of the developed mortise-tenon metamaterials were porous configurations, and traditional processes such as inverted molding and subtractive manufacturing were difficult to meet the preparation requirements, which required the adoption of additive manufacturing methods. The fabrication of metamaterials was performed by conventional additive manufacturing methods to verify the universality of the proposed mortise-tenon design method. The feasibility of fabricating metamaterials such as rigid-SMP UV sensitive resin, polylactic acid-SMP (PLA-SMP) and aluminum alloys with different stiffnesses, as well as fabrication techniques such as LCD photopolymerization printing technology, fused deposition molding, and selective laser melting were verified. Fig. 2B ~ 2D and Figs. S2–S6 demonstrate the integrated metamaterials fabricated by different materials and printing processes, which were fabricated with high accuracy. Movie S3 demonstrates the assembly and disassembly of the mortise-tenon metamaterials. The assembled metamaterials were enabled to fasten discrete parts via the mortise and tenon mechanism, maintaining its configuration and bearing loads. Meanwhile, the discrete structural design strategy endowed the developed metamaterials with highly modular function, which allowed customisation of the configuration/mechanical properties and repair of the metamaterials by replacing the mortise-tenon parts.

Fig. 2E demonstrates the fabrication process of the mechanical-electromagnetic multifunctional metamaterials. The 3D hierarchical network structure was constructed by inserting GO nanosheets between MXene shells. Stabilized MXene@GO dispersions were developed due to the similar hydrophilicity and negative charge of these two materials. Then, the polyvinyl alcohol (PVA) molecular chains were inserted between the MXene@GO nanoshells to form the hydrogel and aerogel with the interpenetrating network structure. The multifunctional metamaterials with brick–mortar structure was fabricated by integrating "brick" (the mortise-tenon metamaterials) with "mortar" (MXene@GO composite aerogel). Fig. 2F exhibits the SEM results of the porous structure with multistage ordered layers of MXene@GO composite aerogel. The porous configuration of the aerogel reduced the weight while increasing the contact area between the electromagnetic wave and

the aerogel, which improved the electromagnetic wave absorption ability. The EDS scans of MXene@GO composite aerogel demonstrated the distribution of the C, O, and Ti, confirming that the MXene was uniformly distributed in the matrix. Fig. 2E and Fig. S2B exhibit the optical image of the fabricated mechanical-electromagnetic multifunctional metamaterials with brick–mortar structure. In the process of freeze-drying to form composite aerogel, the fluidity of the hydrogel precursor was restricted by the mortise-tenon metamaterial, which made the composite aerogel tightly wrapped around the metamaterial to form the composite reinforced structure similar to reinforced concrete structure. In addition, the surface functional groups on the MXene and GO nanosheets (hydroxyl group –OH on MXene and carboxyl group –COOH on GO) were able to form hydrogen bonding interactions with the metamaterial ligaments, which ensured the tight bonding between the metamaterials and the MXene@GO composite aerogel.

2.3. Mechanical properties characterization of mortise-tenon metamaterials

Fig. 3A illustrates the Octet mortise-tenon metamaterial with dimensions $L_x \times L_y \times L_z$, which consists of the connecting parts (Part 3 ~ Part 12) and the main parts (Part 1 and Part 2) with Octet cells. The dimensions of Part1 and Part2 were $L_x \times L_y \times L_{z0}$, which were composed of four $L_{x0} \times L_{y0} \times L_{z0}$ Octet lattice metamaterials and connecting layers (Fig. S1K). The effect of the distribution number of Octet cells along the x ,y, and z directions of the four Octet lattice metamaterials in Part1 and Part2 on the effective mechanical properties of metamaterials was investigated. There were 13 distribution types of the Octet cells, the

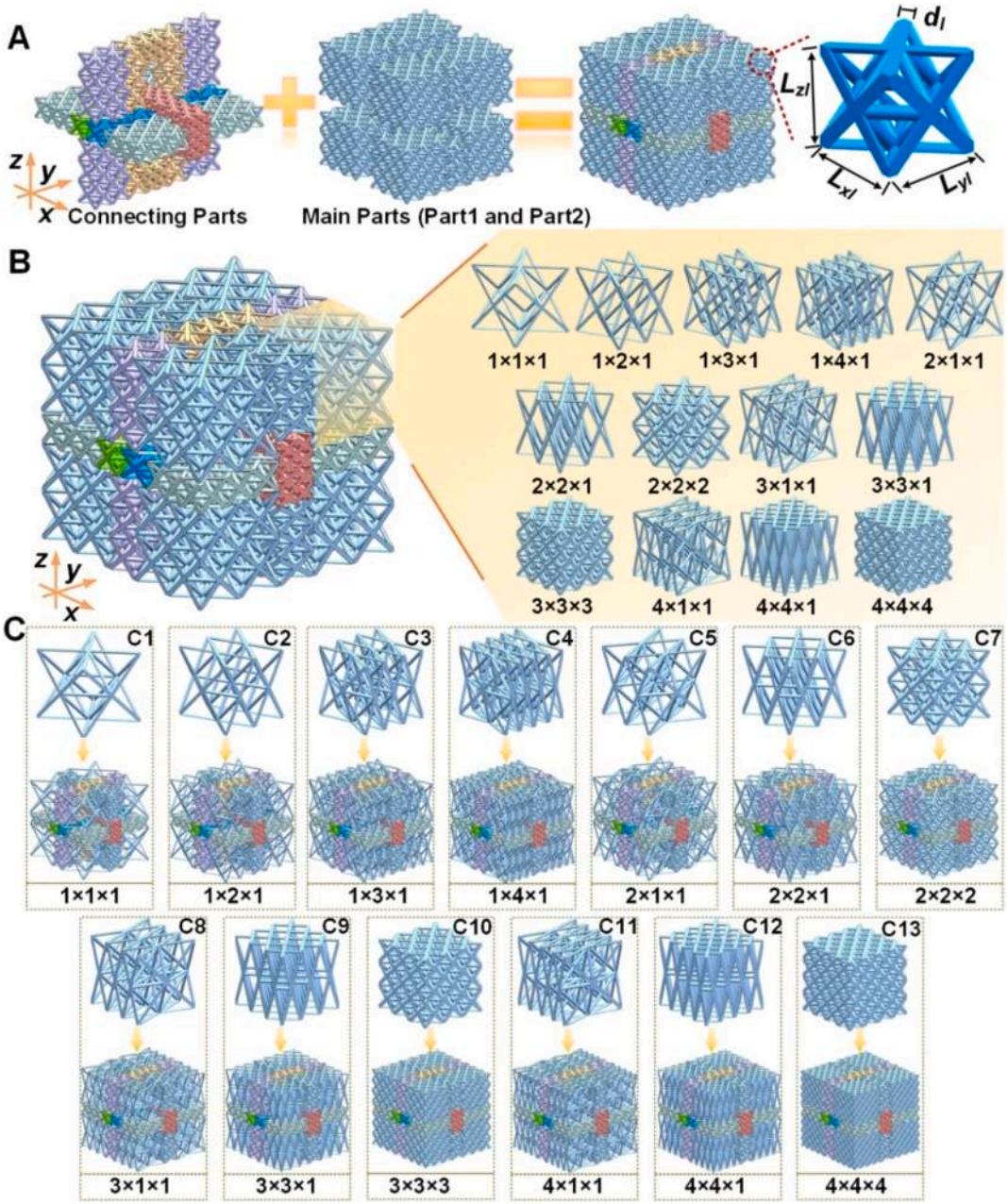

Fig. 3. The design models of the Octet mortise-tenon metamaterials: (A) The metamaterial consisted of connecting parts and main parts (Part1 and Part2), each consisting of Octet-type lattice cells. (B) The main parts (Part1 and Part2) composed of four Octet lattice metamaterials and connecting layers. The 13 types of Octet lattice metamaterials with different geometrical configurations. (C) The Octet mortise-tenon metamaterials consisting of Octet lattice metamaterials with different geometrical configurations.

distribution number of the cells along (x, y, z) direction were (1, 1, 1), (1, 2, 1), (1, 3, 1), (1, 4, 1), (2, 1, 1), (2, 2, 1), (2, 2, 2), (3, 1, 1), (3, 3, 1), (3, 3, 3), (4, 1, 1), (4, 4, 1), (4, 4, 4), respectively (Fig. 3B). The 13 types mortise-tenon metamaterials were obtained by assembling the Part1 ~ Part2 with different geometrical configurations and connecting parts. The 13 types mortise-tenon metamaterials were named according to the distribution number of cells along the x ,y, and z directions in Part1 and Part2 for convenience of description (Fig. 3C). For example, the mortise-tenon metamaterials with (2, 2, 2) distribution of the cells along (x, y, z) in the main parts was named 2 × 2 × 2.

Fig. 4A ~ 4D and Fig. S8 exhibit the compressive displacement-force curves of the developed Octet mortise-tenon metamaterials fabricated by rigid-SMP. The developed metamaterials exhibited different compressive mechanical responses along the x ,y, and z directions due to the different configurations along the x ,y, and z axis (Fig. 4A ~ 4C). When the metamaterial was subjected to the compressive load along the x-axis, the displacement-force curves of the metamaterials with lower density (1 × 1 × 1 and 2 × 2 × 2) exhibited the initial linear elasticity region, plateau stress region, and the rapidly increasing densification region (Fig. 4A). The displacement-force curves of metamaterials with higher density (3 × 3 × 3 and 4 × 4 × 4) exhibited the initial linear elastic region, followed by the load decreasing stage. This phenomenon was due to that as the increase of the Octet cells density, the plateau region load was higher than the fracture load of the mortise-tenon parts, leading to fracture and collapse of the connecting parts.

When the Octet mortise-tenon metamaterials were subjected to compressive loads along the z- and y-axis, the displacement-force curves of the developed metamaterials exhibited elastic region, plateau region and densification region, as shown in Fig. 4B ~ 4D. The mortise-tenon metamaterials joined discrete parts of each other into the whole by

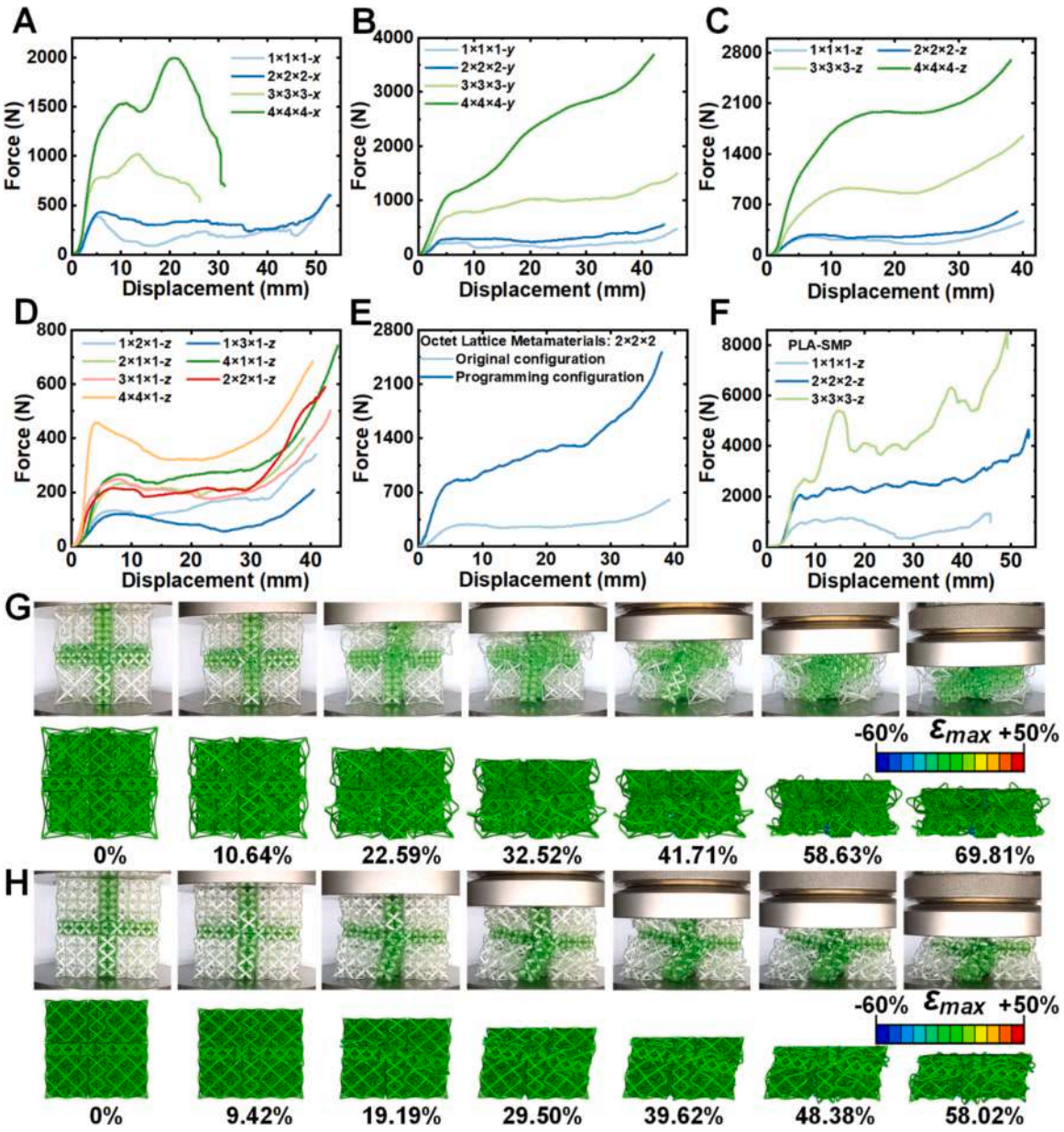

Fig. 4. The mechanical properties of the developed Octet mortise-tenon metamaterials with different geometrical configurations. Compressive displacement-force curves of the metamaterial along (A) x , (B) y, and (C) z axis. (D) The compressive properties along the z-axis of metamaterials with cells gradient distribution. (E) The programmability of the mechanical properties of metamaterials under compressive loading by shape memory properties. (F) Compressive properties along the z-axis of metamaterials fabricated by PLA-SMP. The comparison results of the optical images with FEA of the deformation process of the metamaterials under compressive loading along the z-axis: (G)1 × 1 × 1; (H) 2 × 2 × 2.

mortise-tenon connection method. The metamaterial first produced elastic deformation under compression load, which led to smaller fitting gaps between the connecting parts, and improved the integrity of the metamaterial, so that the metamaterial remained integral during the deformation process. The ligaments in the metamaterial produced buckling and plastic deformation with further increase of the load, which led to the plateau region in its compressive displacement-force curve. The metamaterial entered the densification region due to the mutual contact between the ligaments. The area enclosed by the elastic and platform regions represented the energy absorption ability. Among the 3 directions, the metamaterials along the *z*-axis realized energy-absorbing characteristics (Fig. S12). The load values of the plateau region of the metamaterial increased with the increase of the density of the cells.

Fig. 4G ~ 4H and Fig. S9 demonstrate the deformation process of the metamaterial subjected to *z*-axis compressive loading, which the finite element analysis (FEA) reproduced with high accuracy. Fig. S9 exhibits the distribution of maximum principal strains and Mises stresses in the mortise and tenon metamaterials under different deformations. The cells in the mortise-tenon metamaterials reached the yield stress of the parent material, which caused the Octet cells underwent flexural deformation and collapse. During the compression process, the connecting parts connected to the main parts and mortised with each other to maintain the configuration of the metamaterial. The integrity and mechanical properties of the mortise-tenon metamaterials were relatively poor compared with the seamlessly printed and non-assembly method methods. In the compression process, the maximum principal strain and maximum Mises stress of the mortise-tenon metamaterial appeared at the joints between the connecting parts. This was mainly due to the fact that the mortise- −tenon parts were in contact and extruded with each other, which led to the stress concentration phenomenon in each part, reducing the mechanical properties and stability of the metamaterial. However, the mortise-tenon metamaterials were able to maintain the interconnected configuration and exhibit energy-absorbing properties during the compressive deformation process. It was worth noting that the connecting parts were composed of Octet cells, which exhibited the same mechanical properties as the main parts.

The developed metamaterials exhibited programmable and reconfigurable properties of the configuration and mechanical properties, utilizing the shape memory properties. The specific implementation of shape memory programming and reconfiguration of metamaterials was as follows: 1) Heating and loading: The metamaterial with the original configuration was heated above the glass transition temperature (Tg) and then deformed by the applied loads (ε_a, applying circumferential compressive loads in this work); 2) Cooling and unloading: While maintaining the deformation ε_a, the metamaterial was cooled to room temperature. 3) Load independent (i.e., programmability): The metamaterial maintained the programmed configuration (i.e., ε_{target}) after unloading and carried external loads. The geometrical parameters of metamaterials with the programmed configuration were different from those of the original configuration, resulting in different mechanical properties to the original configuration (i.e., programmability of mechanical). In the ε_{target}, the mortise-tenon metamaterial still enabled the high connection strength and maintained its configuration. 4) Reheating and recovery: When the temperature was reheated to T_g, the metamaterials were recovered from its programmed configuration to its original configuration, resulting in the mechanical properties recovering to its original state (i.e., reconfigurability, Movie S4). Compared with typical metamaterials, 4D-printed metamaterials exhibited properties such as reconfigurable configurations, tunable mechanical properties, and self-adaptation, which improved the design freedom of metamaterials. Fig. 4E demonstrates the programmable properties of the compressive displacement-force curves of the mechanical metamaterials. It was worth noting that the metamaterials were programmed under circumferential compressive loading. The cells of the metamaterials with temporary configurations were compacted, leading to the programmed metamaterials with high stiffness. When subjected to compression along the *z*-axis, the energy absorption of the metamaterials with the original and programmed configurations was ~ 7.6 kJ and 26.5 kJ, respectively (Fig. S13).

The metamaterials with rigid-SMP were able to maintain the whole conformation during deformation due to the high toughness of rigid-SMP (Young's modulus ~ 300 MPa, fracture strain ~ 40 %). The flexibility of the rigid-SMP enabled the mortise-tenon connecting parts to deform together. Even if the connecting parts were deformed significantly, it still allowed the parts to mortise into each other to maintain the whole configuration. In addition, the compressive mechanical response of the Octet mortise-tenon metamaterials fabricated by low-toughness materials (PLA-SMP, Young's modulus ~ 1.4 GPa, fracture strain ~ 9 %[14]) was also characterized, as shown in Fig. 4F and Fig. S10. Compared with rigid-SMP, PLA-SMP possessed higher Young's modulus. Therefore, the PLA-SMP Octet mortise-tenon metamaterials exhibited higher effective stiffness and energy-absorption properties (Fig. S12). It can be obtained from the mechanical property characterization that the components of the developed mortise-tenon metamaterials still maintain high connection performance for materials with low-toughness materials.

The Kelvin, 3D Re-entrant, and 3D chiral mortise-tenon metamaterials fabricated by rigid-SMP were developed to verify the universality of the proposed design strategy (Fig. 5A). Similar to the Octet mortise-tenon metamaterials, the Kelvin, 3D Re-entrant, and 3D chiral mortise-tenon metamaterials were composed of connecting and main parts, which each part composed of the corresponding metamaterial cells. Fig. 5B ~ 5G demonstrate the compressive properties of the metamaterials with different cell types. During compression along *y* and *z* axis, the displacement-force curves of the metamaterials with lower density exhibited elasticity region, plateau region and densification region, while the metamaterials exhibited higher connection strength along the *z*-axis. In particular, metamaterials with 3D Re-entrant cells exhibited plateau regions under compressive loading along the *z*-axis, resulting in better energy absorption properties (Fig. S12).

2.4. Mechanical properties characterization of mechanical-electromagnetic MPM

The multiple mortise-tenon metamaterials were mortised to each other by arraying specific connecting parts, to achieve large-scale, modular integration of the mechanical metamaterials. There were four connection modes from Connection mode I to Connection mode IV. **Connection mode I** (full-size connecting parts): The full-size of the bi-directional six-connected parts were obtained by arranging Part3 and Part4, Part5 and Part6, Part10 and Part12 along the *x* ,*y*, and *z* directions, respectively, where the numbers of arrays were the same as the number of the mortise-tenon metamaterials contained in this direction (Fig. 6A and Fig. S11A). **Connection mode II** (modular connecting parts): The modular unidirectional six-connected parts (modular connecting parts) were obtained by arraying two of Part3 and Part4, Part5 and Part6, Part10 and Part12 along *x* ,*y*, and *z* directions, respectively. Modular connecting parts were arranged in a staggered manner to achieve stable connection between mortise-tenon metamaterials (Fig. 6B and Fig. S11B). The Connection mode I utilized full-size connecting parts, resulting in the fabrication size of the metamaterials limited by the fabrication platform. In contrast to Connection mode I, the fabrication of modular connected parts was not limited by manufacturing dimensions and exhibited standardization and modularity, enabling large-scale and scaled-up fabrication of metamaterials. However, the assembly process of Connection mode II was too cumbersome for rapid repair and modular integration of metamaterials. For the connection performance of mortise-tenon metamaterials, the connection strength and stability of Connection mode I were higher than that of Connection mode II, which was due to the fact that Connection mode I utilized full-size connecting parts while Connection mode II used

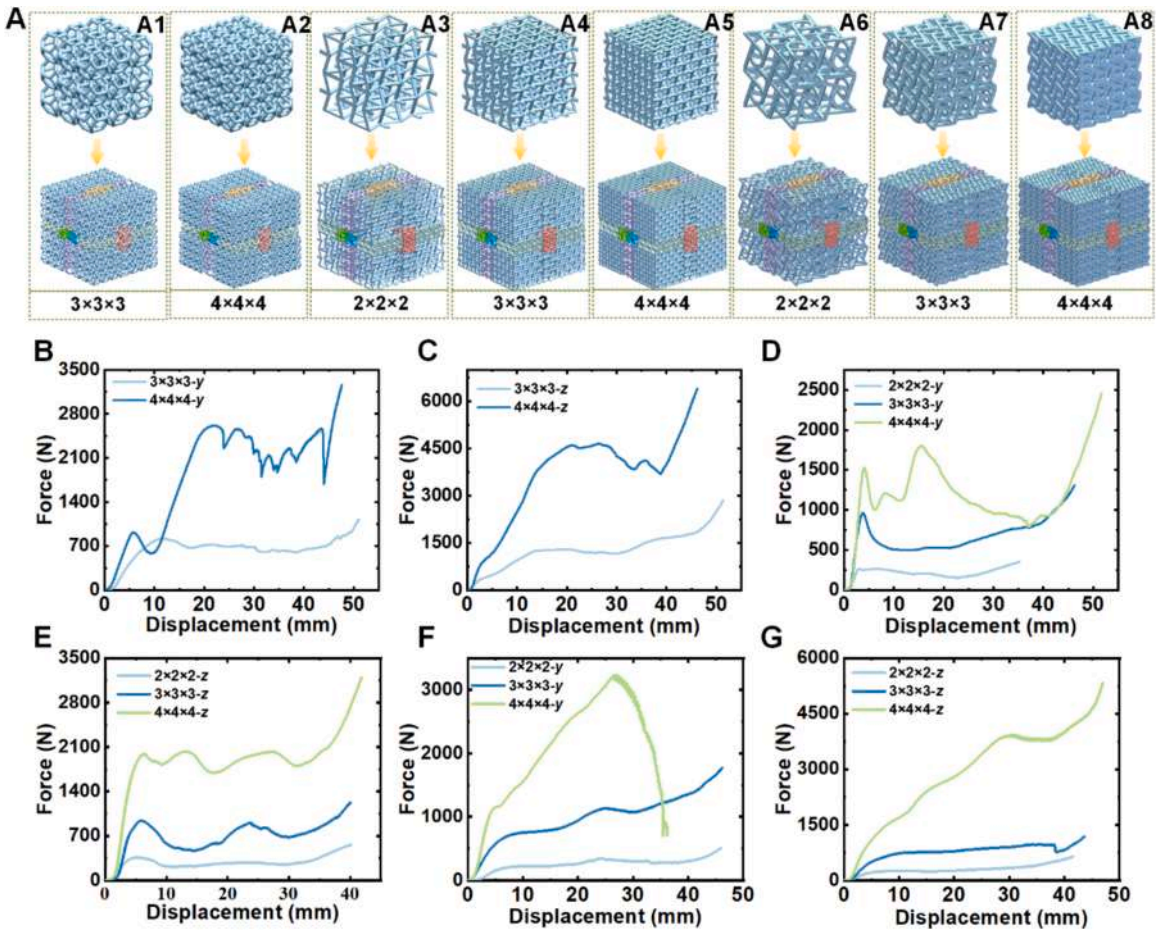

Fig. 5. (A) The developed Kelvin, 3D Re-entrant, and 3D chiral mortise-tenon metamaterials with different geometric configurations. The compressive mechanical properties of Kelvin mortise-tenon mechanical metamaterials: (B) *y*-direction, (C) *z*-direction. The compressive mechanical properties of 3D Re-entrant mortise-tenon mechanical metamaterials: (D) *y*-direction, (E) *z*-direction. The compressive mechanical properties of 3D chiral mortise-tenon mechanical metamaterials: (F) *y*-direction, (G) *z*-direction.

alternate connecting parts.

Connection mode III (pixel type connection along *z*-axis): The pixel type connection along the *z*-axis consisting of unidirectional double connection parts and cable ties was obtained by removing the *x*- and *y*-direction connection parts in Connection mode II. The MP was developed by connecting multiple mortise-tenon metamaterials applying Connection mode III. The MPM with stabilized connections were constructed by tying the discrete MPs (Fig. S11C–D). **Connection mode IV** (pixel type connection along *x*-axis or *y*-axis): The pixel type connection methods along the *x*- or *y*-directions were obtained by removing the *y*-/*z*-direction or *x*-/*z*-direction connection parts in Connection mode II (i.e., modular connecting parts of Part 3 and Part 4), respectively. The CAD models of modular connecting parts of Part 3 and Part 4 are shown in Table S1. Movie S2 demonstrates the assembly process of MP by connecting 3 mortise-tenon metamaterials utilizing Connection mode IV. Then the discrete MPs were connected to form the MPM utilizing the bundling method. Fig. 6C ~ 6D and Fig. S11E–F illustrate the pixel type connection along *x*-axis. Due to the high load-bearing capacity of mortise-tenon metamaterials along the z −axis, the optimal load-bearing direction for MPM was along the *z*-axis. Connection mode III was the alternate distribution of modular connecting parts along the *z*-axis (i.e., MPs were distributed in the *xy*-plane). When the MPM with connection mode III was subjected to the compressive load along the *z*-axis, the MP was subjected to buckling deformation (slender beam) along the *z*-axis, which reduced the structural stability and the load carrying capacity of the MPM. The Connection mode IV was the alternating distribution of modular connecting parts along the *x*-axis/*y*-axis (i.e., MPs were distributed along the *yz*/*xz* plane). MPM was the short beam with high stability when it was subjected to compression load along the z-axis. Therefore, the MPM integrated by Connection mode IV possessed higher connection performance compared to Connection mode III.

The scalable and modular MPs were designed by connecting $n_p = 3$ Octet mortise-tenon metamaterials ($2 \times 2 \times 2$ and $3 \times 3 \times 3$) via Connection mode IV, as shown in Fig. 6E. The MPs with different mechanical properties were obtained by integrating mortise-tenon metamaterials with different configurations (Fig. 6F). The MPM was developed by arraying the MPs along the *y*-axis and *z*-axis and tied with cable ties. Fig. 6G illustrates the mortise-tenon MPMs consisting of $3 \times 3 \times 3$ and $2 \times 2 \times 2$ Octet mortise-tenon metamaterials (MPM_{III} and MPM_{II}), respectively, each MPM containing 9 MPs (i.e., 27 Octet mortise-tenon metamaterials).

The displacement-force curves of the MPM exhibited contact, elastic, plateau, and densification regions under compressive loading along the *z*-axis (Fig. 6H). In the initial stage, the MPs contacted each other under compressive loading and formed the force-transfer paths. The MPM underwent elastic deformation as the load increased until the ligaments buckled, resulting in the plateau region in the displacement-force curve. The MPM was compacted with the increase of load, leading to the significant increase in its effective stiffness (i.e., densification region). The plateau region load values of MPM_{III} was higher than that of MPM_{II}, which was attributed to the higher density of cells in MPM_{III}. The energy absorption (EA) of MPM_{II} and MPM_{III} was ~ 1222.0 kJ and 2296.1 kJ, respectively (Fig. S14).

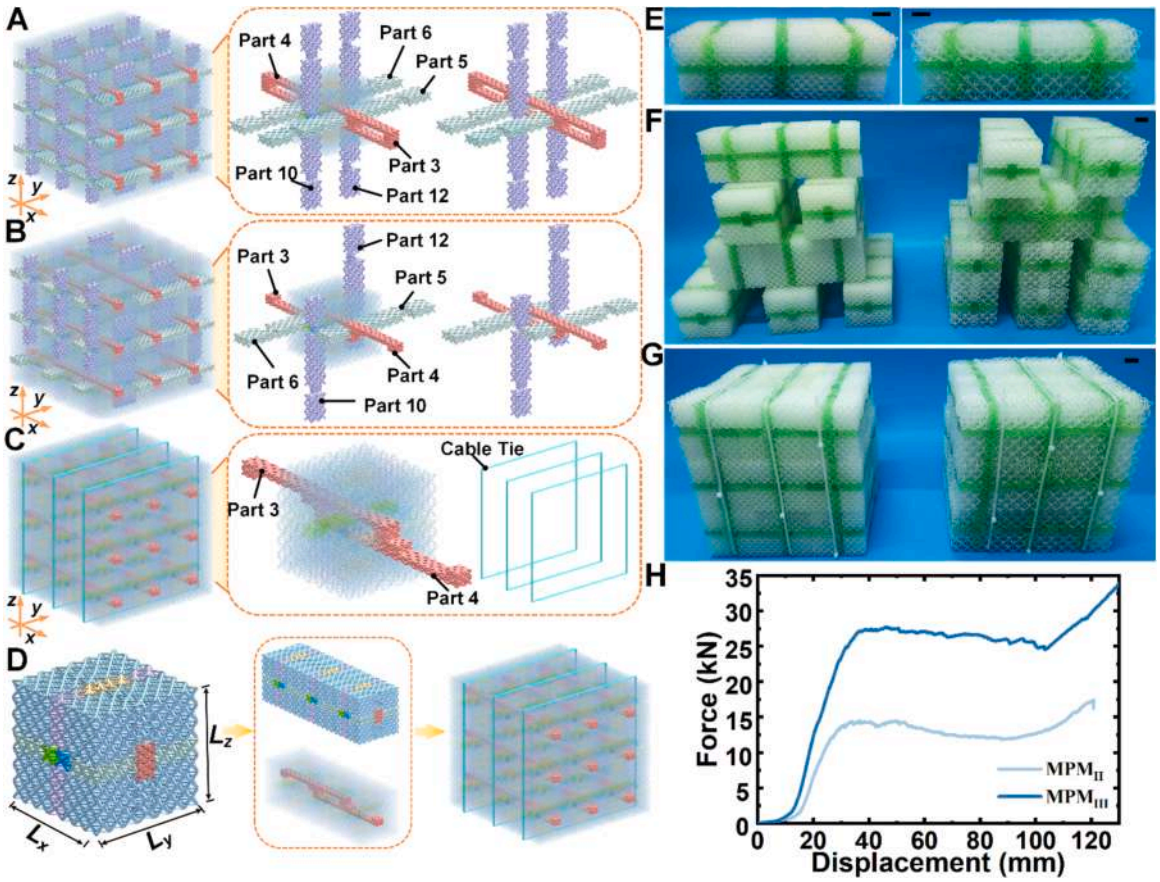

Fig. 6. Mortise-tenon metamaterials with different connection modes: (A) Connection mode I, (B) Connection mode II, (C) Connection mode IV. (D) The MPs were integrated by employing Connection mode IV to connect multiple mortise-tenon metamaterials, and the MPMs were fabricated by arraying multiple MPs and bundling. (E) The MPs were designed by connecting 3 Octet mortise-tenon metamaterials via Connection mode IV. (F) The MPs with different geometrical configurations. (G) The developed MPM: The MPM consisting of $3 \times 3 \times 3$ (left, MPM_{III}) and $2 \times 2 \times 2$ (right, MPM_{II}) Octet mortise-tenon mechanical metamaterials. (H) The compression displacement-force curves of the MPM_{III} and MPM_{II} . The scale bar is 20 mm.

2.5. Electromagnetic properties and application prospects of mechanical-electromagnetic MPM

Fig. 7A demonstrates the variation of the complex permittivity ($\varepsilon = \varepsilon'$-j$\varepsilon''$) of the "mortar" of mechanical-electromagnetic MPM (Mxene@GO composite aerogel) in the frequency range of 1–18 GHz. ε' and ε'' denoted the storage and attenuation of electromagnetic energy, respectively. The loss tangent ($\tan \delta_\varepsilon = \varepsilon''/\varepsilon'$) was utilized to represent the dielectric loss ability of the composite aerogel. The ε' and ε'' of composite aerogel decreased with the increase of frequency, demonstrating its favorable frequency dispersion characteristics. The $\tan \delta_\varepsilon$ values ranging from 0.57 to 0.12 indicated that the composite aerogel exhibited excellent dielectric loss ability (Fig. 7A). The EMW dissipation mechanism of the composite aerogel was primarily via dielectric loss owing to the unadded magnetically sensitive particles. The dielectric loss consisted of polarization loss and conductive loss according to the basic mechanism of EMW attenuation. The dipolar polarization was attributed to asymmetric charge distribution caused by structural defects and heteroatomic dopants. Repeated rotation of the electric dipole with the asymmetric charge distribution led to polarization relaxation behavior due to its inability to change in synchrony with the frequency of the alternating electromagnetic field. The conductive loss acted as an attenuating factor of electromagnetic energy for conductive EMW absorbing materials. The induced microcurrent (magnetic field-induced eddy currents and electric field-induced currents) contributed to the conversion of electromagnetic energy into Joule heat under the electromagnetic field. In addition, the porous configuration of the aerogel enabled the EMW to be reflected and absorbed multiple times in the voids, realizing the efficient absorption of EMW. The reflection loss (RL) of the aerogel with different thicknesses was evaluated in the frequency range of 1–18 GHz (Fig. 7B ~ 7C). The MXene@GO composite aerogel exhibited the significant RL_{min} value of −43.81 dB at 2.2 mm thickness and 12.75 GHz.

The mechanical-electromagnetic MPM was developed by combining MPs ($n_p = 1$) and cable tie. The RL of developed MPM in the frequency range of 1 ~ 18 GHz was evaluated along the perpendicular to the aerogel filling direction (Fig. 7D). The porous characteristics of the mechanical-electromagnetic MPM were able to scatter the incident electromagnetic waves and absorbed by the MXene@GO composite aerogel. The porous configuration of MXene@GO composite aerogel resulted in the reciprocal reflection and absorption of electromagnetic waves in the pores, realizing the highly efficient absorption of electromagnetic waves. When the RL was less than −10 dB, the absorbing material exhibited at least 90 % of the electromagnetic loss. Therefore, the mechanical-electromagnetic MPM possessed more than 90 % electromagnetic loss capability in the frequency range of 9.86 GHz ~ 14.40 GHz and 14.81 GHz ~ 15.66 GHz (Fig. 7E). The RL_{min} value of the mechanical-electromagnetic MPM was –32.84 dB at 15.28 Hz(Fig. 7E). It was worth noting that the mechanical and electromagnetic functions of the developed mechanical-electromagnetic MPM were realized by mortise-tenon metamaterials and MXene@GO composite aerogel, respectively. The aerogel had the porous configuration, which had relatively poor mechanical properties and had small effect on the overall mechanical properties of the metamaterials. The absorption ability of the mechanical-electromagnetic MPM for vertically incident electromagnetic waves was demonstrated in this work, due to the filling direction of the aerogel and the optimal load bearing direction of the

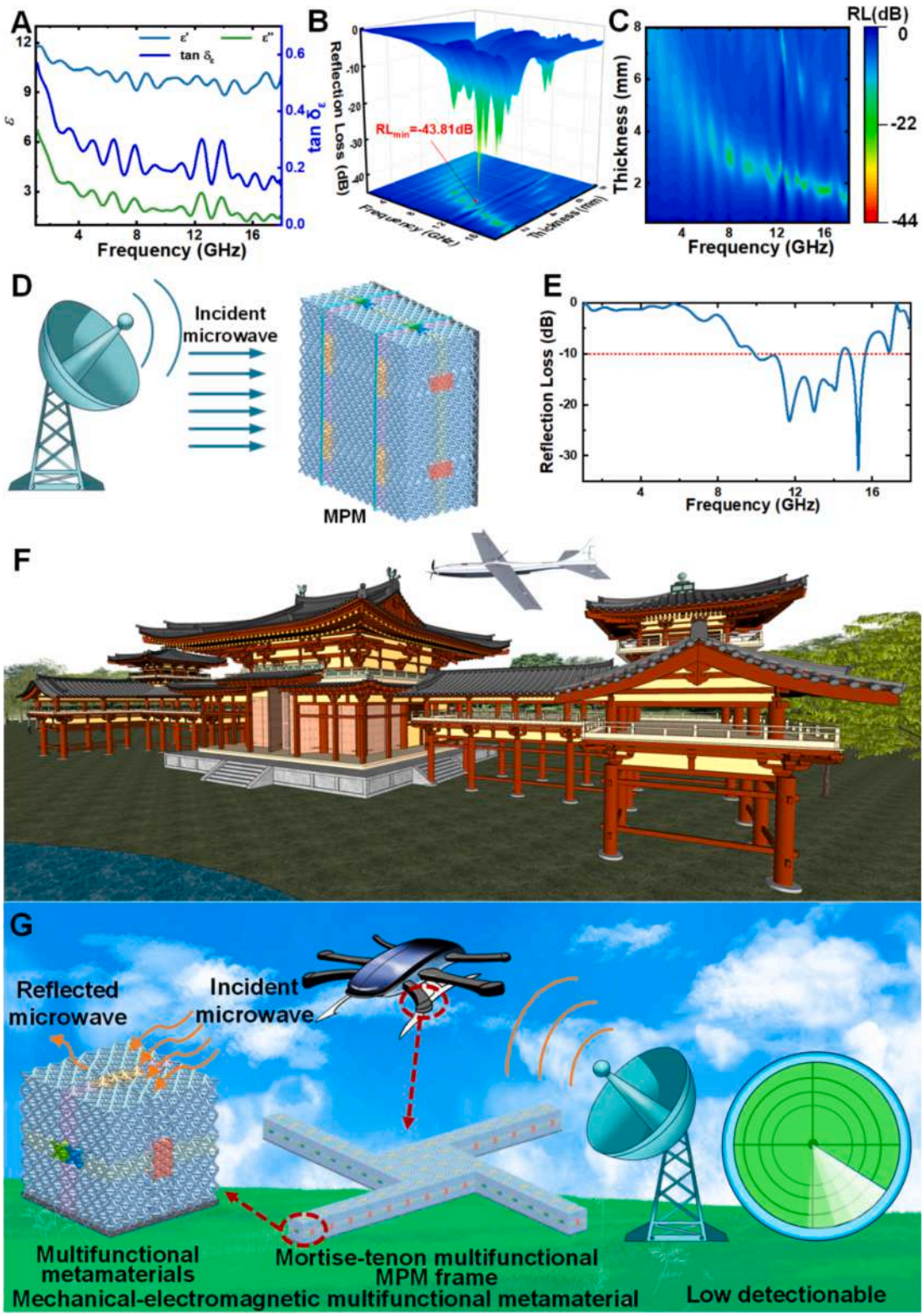

Fig. 7. (A) The dielectric loss properties of the MXene@GO composite aerogel. (B) 3D representation and (C) 2D representation of RL values of composite aerogels with different thicknesses at 1–18 GHz. The (D) schematic and (E) RL of the EMW absorption performance test of mechanical-electromagnetic MPM. (F)~(G) The developed mechanical-electromagnetic MPM possessed the wide application prospect in the UAVs and absorber.

mortise-tenon metamaterials were both in the z-axis.

The mortise-tenon connection type developed in this work had the ability to satisfy different printing methods and materials. Through efficient, low-cost production and highly reproducible assembly process, the metamaterials eliminated scale limitations and realized ultra-large dimensions beyond the fabrication scale of 3D printers. The mortise-tenon discrete assembly provided several benefits which distinguished it from existing manufacturing methods for the metamaterials, including increased functionality, repairability, reconfigurability, and scalability. Due to the discrete characteristics of the structure, damaged parts can be

removed and replaced. The key to the mass commercial application of mortise-tenon metamaterials is automated assembly. By combining automated assembly methods, it is foreseen that this research will hold promise for realizing metamaterials on the macro scale. The developed mechanical-electromagnetic MPM possessed modularity, lightweight, energy absorption and electromagnetic absorption capabilities, providing potential applications in the electromagnetic stealth equipment. For example, the frame structure of the low-detection UAV can be designed utilizing the developed mechanical-electromagnetic metamaterials, realizing electromagnetic stealth characteristics while meeting the lightweight and load-carrying functions of the UAV (Fig. 7F and Fig. 7G). The UAV architecture was integrated and fixed by mortising and tenoning the components to ensure its mechanical properties. The mechanical-electromagnetic MPM converted the incident EMW into other energies, such as heat, to achieve the dissipation of EMW. In addition, mechanical-electromagnetic MPM exhibited the potential to replace metal shells utilized for electromagnetic interference (EMI) shielding to absorb microwave noise signals generated by UAV.

3. Experimental section

3.1. Design and fabrication of mechanical metamaterials

The CAD models of the metamaterials were constructed by Siemens PLM Software UG NX10.0 and exported in "stl" file format. The resin-based and metal-based metamaterials were fabricated utilizing UV light-cured LCD printing technology, FDM printing technology and SLM technology. The dimensional fit between the parts of the mortise-tenon metamaterial was realized through multiple iterations of design and high-precision preparation. The design process for metamaterials was as follows: The CAD model of the mortise-tenon component was established in UG NX software, and then the mortise-tenon metamaterial was assembled in the assembly mode of the software (Movie-S1 and Movie-S2). In the assembled CAD model, we observed whether there was mutual interference and excessive clearance between the mortise-tenon parts, and modified the CAD model. Subsequently, the mortise-tenon parts were fabricated and assembled, and the relevant parameters of the CAD model were adjusted again according to the printed objects.

3.2. The characterization and simulation of compression properties of metamaterials

The nonlinear behavior of metamaterials was investigated by the Zwick-010 tensile machine with an environmental chamber and the compression rate was 2 mm min^{-1}. The camera (Canon DS126571) was utilized to record the optical images of the metamaterials during the testing process. The commercial finite element software ABAQUS (3DS Dassault Systèmes, France) was employed to calculate the nonlinear deformation behavior of the developed metamaterials.

3.3. The fabrication of MXene@GO composite aerogels

Polyvinyl alcohol (PVA, 1788), as the phase of matrix and encapsulation, was obtained from Aladdin Chemical Reagent Co., Ltd. (Shanghai, China). The MXene nanoshell with the diameter of 2 ~ 50 μm, was purchased from Xinxi Technology Co., Ltd. (Foshan, China). The Graphene oxide (GO) dispersion, with the concentration of 10 mg mL^{-1}, was utilized to form an interlayer network and purchased from Maclin Biochemical Co., Ltd. (Shanghai, China). The GO dispersion was diluted to 2 mg mL^{-1}, and 40 mL of the GO dispersion was sonicated for 2 h and then MXene nanosheets were added to it (MXene:GO = 5:1). Subsequently, the mixed solution was sonicated for 1 h and then magnetically stirred at room temperature for 2 h, resulting in the insertion of GO nanosheets into the interlayers of MXene sheets, thereby forming a 3D hierarchical network structure to form the MXene@GO dispersion. The PVA powder was added to the above mixed solution and magnetically stirred at 90 °C for 2 h, resulting in the insertion of PVA molecular chains between the MXene@GO nanosheets to form the hydrogel precursor solution. The hydrogel precursor solution was poured into the mold where the mechanistic metamaterial was placed to fill the voids of the metamaterial structure, and the hydrogel EMW-absorbing layer was formed on the bottom surface of the metamaterial after three freeze–thaw cycles. Finally, the MPM with brick–mortar structure were constructed by freeze-drying method.

3.4. The electromagnetic properties of MXene@GO aerogels and mechanical-electromagnetic MPM

MXene@GO composite aerogel scattering parameters (S11, S12, S21, and S22) were measured by the vector network analyzer (E5071C) in the frequency range 1–18 GHz. The values of electromagnetic parameters such as complex permittivity (ε', ε'') were obtained according to the S-parameters. RL was calculated based on transmission line theory as follows:

$$RL = 20\log\left|\frac{Z_{in} - Z_0}{Z_{in} + Z_0}\right|$$

$$Z_{in} = Z_0\sqrt{\frac{\mu}{\varepsilon}}\tanh\left(j\frac{2\pi fd}{c}\sqrt{\varepsilon\mu}\right)$$

where, Z_0 and Z_{in} were the free-space impedance and absorber input impedance, respectively. c was the light velocity, and f represented the thickness.

The RL of mechanical-electromagnetic MPM was measured utilizing the bow method reflectance test system (Fig. 7D). The test equipment mainly included transmitting antenna, receiving antenna, bow frame, transmission cable, metal sample platform, cone-shaped EMW-absorbing material, and network vector analyzer, etc. The mechanical-electromagnetic MPM (180 mm × 180 mm × 87 mm) was placed on the sample platform and in the center of the bow frame. The transmitting and receiving antennas were mounted on bow frames which were suspended above the sample platform.

4. Conclusion

In summary, the mortise-tenon mechanical-electromagnetic multifunctional metamaterial were developed in this work to overcome the limitations of the lack of modularity, large-scale fabrication and single functionality suffered by mechanical metamaterials. The mortise-tenon metamaterial can be interlocked with each other to withstand external loads while maintaining the configuration of the metamaterial. Most importantly, the MPs in the mechanical-electromagnetic MPM enabled the transmission of loads to each other, while demonstrating the advantages of modularity, no redundant connection structure, serviceability, and scalable manufacturing. The mechanical and electromagnetic properties of the mechanical-electromagnetic MPM in energy absorption, integrated material-structure–function EMW absorber were verified, which possessed a wide application prospect in the electromagnetic stealth equipment.

CRediT authorship contribution statement

Xiaozhou Xin: Writing – original draft, Software, Methodology, Formal analysis. **Chunli Yang:** Methodology, Investigation. **Zhicheng Wang:** Visualization, Methodology. **Yin Xing:** Software, Investigation. **Chengjun Zeng:** Writing – review & editing, Software. **Liwu Liu:** Writing – review & editing, Funding acquisition. **Yanju Liu:** Writing – review & editing, Funding acquisition. **Jinsong Leng:** Project administration, Funding acquisition.

Declaration of competing interest

The authors declare that they have no known competing financial interests or personal relationships that could have appeared to influence the work reported in this paper.

Acknowledgements

The authors gratefully acknowledge the financial support provided by the National Key R&D Program of China (2022YFB3805700), the National Natural Science Foundation of China (Grant Nos. 12402185, 12072094 and 12172106), the China Postdoctoral Science Foundation (Grant Nos. 2023M730869), the Heilongjiang Natural Science Foundation Joint Guidance Project (Grant Nos. LH2023A004), the Open Foundation of Key Laboratory of Multi-spectral Absorbing Materials and Structures (KPKFJJ20250011-1).

Appendix A. Supplementary material

Supplementary data to this article can be found online at https://doi.org/10.1016/j.cej.2024.158784.

Data availability

Data will be made available on request.

References

[1] G. Bordiga, E. Medina, S. Jafarzadeh, C. Bösch, R.P. Adams, V. Tournat, K. Bertoldi, Automated discovery of reprogrammable nonlinear dynamic metamaterials, Nat. Mater. (2024), https://doi.org/10.1038/s41563-024-02008-6.
[2] Y. Liu, Y.Z. Wang, H.Y. Ren, Z.Q. Meng, X.Q. Chen, Z.Y. Li, L.W. Wang, W. Chen, Y. F. Wang, J.B. Du, Ultrastiff metamaterials generated through a multilayer strategy and topology optimization, Nat Commun 15(1) (2024). https://doi.org/ARTN 2984 10.1038/s41467-024-47089-8.
[3] X. Huang, W. Guo, S.Y. Liu, Y.Y. Li, Y.Q. Qiu, H. Fang, G.G. Yang, K.H. Zhu, Z.P. Yin, Z. Li, H. Wu, Flexible Mechanical Metamaterials Enabled Electronic Skin for Real-Time Detection of Unstable Grasping in Robotic Manipulation, Adv Funct Mater 32(23) (2022). https://doi.org/ARTN 210910910.1002/adfm.202109109.
[4] J. Li, R.H. Bao, W.Q. Chen, Exploring static responses, mode transitions, and feasible tunability of Kagome-based flexible mechanical metamaterials, J Mech Phys Solids 186 (2024). https://doi.org/ARTN 10559910.1016/j.jmps.2024.105599.
[5] I. Fernandez-Corbaton, C. Rockstuhl, P. Ziemke, P. Gumbsch, A. Albiez, R. Schwaiger, T. Frenzel, M. Kadic, M. Wegener, New Twists of 3D Chiral Metamaterials, Adv Mater 31(26) (2019). https://doi.org/ARTN 180774210.1002/adma.201807742.
[6] T. Frenzel, M. Kadic, M. Wegener, Three-dimensional mechanical metamaterials with a twist, Science 358 (6366) (2017) 1072–1074, https://doi.org/10.1126/science.aao4640.
[7] T. Chen, M. Pauly, P.M. Reis, A reprogrammable mechanical metamaterial with stable memory, Nature 589 (7842) (2021) 386–390, https://doi.org/10.1038/s41586-020-03123-5.
[8] P.C. Jiao, J. Mueller, J.R. Raney, X.Y. Zheng, A.H. Alavi, Mechanical metamaterials and, Nat Commun 14(1) (2023). https://doi.org/ARTN 600410.1038/s41467-023-41679-8.
[9] D. Melancon, B. Gorissen, C.J. Garcia-Mora, C. Hoberman, K. Bertoldi, Multistable inflatable origami structures at the metre scale, Nature 592 (7855) (2021) 545–550, https://doi.org/10.1038/s41586-021-03407-4.
[10] H. Zhang, J. Wu, D.N. Fang, Y.H. Zhang, Hierarchical mechanical metamaterials built with scalable tristable elements for ternary logic operation and amplitude modulation, Sci Adv 7(9) (2021). https://doi.org/ARTN eabf196610.1126/sciadv.abf1966.
[11] M. Zaiser, S. Zapperi, Disordered mechanical metamaterials, Nat. Rev. Phys. 5 (11) (2023) 679–688, https://doi.org/10.1038/s42254-023-00639-3.
[12] A.E. Forte, D. Melancon, M. Zanati, M. De Giorgi, K. Bertoldi, Chiral mechanical metamaterials for tunable optical transmittance, Adv. Funct. Mater. 33 (20) (2023), https://doi.org/10.1002/adfm.202214897.
[13] C. Yang, M. Boorugu, A. Dopp, J. Ren, R. Martin, D. Han, W. Choi, H. Lee, 4D printing reconfigurable, deployable and mechanically tunable metamaterials, Mater. Horiz. 6 (6) (2019) 1244–1250, https://doi.org/10.1039/c9mh00302a.
[14] X.Z. Xin, L.W. Liu, Y.J. Liu, J.S. Leng, 4D Printing Auxetic Metamaterials with Tunable, Programmable, and Reconfigurable Mechanical Properties, Adv Funct Mater 30(43) (2020). https://doi.org/ARTN 200422610.1002/adfm.202004226.
[15] F. Pan, Y.L. Li, Z.Y. Li, J.L. Yang, B. Liu, Y.L. Chen, 3D Pixel Mechanical Metamaterials, Adv Mater 31(25) (2019). https://doi.org/ARTN 190054810.1002/adma.201900548.
[16] X.Z. Xin, L.W. Liu, Y.J. Liu, J.S. Leng, 4D Pixel Mechanical Metamaterials with Programmable and Reconfigurable Properties, Adv Funct Mater 32(6) (2022). https://doi.org/ARTN 210779510.1002/adfm.202107795.
[17] X. Kuang, D.J. Roach, J.T. Wu, C.M. Hamel, Z. Ding, T.J. Wang, M.L. Dunn, H.J. Qi, Advances in 4D Printing: Materials and Applications, Adv Funct Mater 29(2) (2019). https://doi.org/ARTN 180529010.1002/adfm.201805290.
[18] P. Fu, H.M. Li, J. Gong, Z.J. Fan, A.T. Smith, K.Y. Shen, T.O. Khalfalla, H.F. Huang, X. Qian, J.R. McCutcheon, L.Y. Sun, 4D printing of polymers: Techniques, materials, and prospects, Prog Polym Sci 126 (2022). https://doi.org/ARTN 10150610.1016/j.progpolymsci.2022.101506.
[19] M. Chen, M. Gao, L.C. Bai, H. Zheng, H.J. Qi, K. Zhou, Recent advances in 4D printing of liquid crystal elastomers, Adv. Mater. 35 (23) (2023), https://doi.org/10.1002/adma.202209566.
[20] R. Wang, C. Yuan, J.X. Cheng, X.N. He, H.T. Ye, B.C. Jian, H.G. Li, J.M. Bai, Q. Ge, Direct 4D printing of ceramics driven by hydrogel dehydration, Nat Commun 15(1) (2024). https://doi.org/ARTN 75810.1038/s41467-024-45039-y.
[21] B. Zhang, H.G. Li, J.X. Cheng, H.T. Ye, A.H. Sakhaei, C. Yuan, P. Rao, Y.F. Zhang, Z. Chen, R. Wang, X.N. He, J. Liu, R. Xiao, S.X. Qu, Q. Ge, Mechanically Robust and UV-Curable Shape-Memory Polymers for Digital Light Processing Based 4D Printing, Adv Mater 33(27) (2021). https://doi.org/ARTN 210129810.1002/adma.202101298.
[22] J.X. Fan, L. Zhang, S.S. Wei, Z. Zhang, S.K. Choi, B. Song, Y.S. Shi, A review of additive manufacturing of metamaterials and developing trends, Mater. Today 50 (2021) 303–328, https://doi.org/10.1016/j.mattod.2021.04.019.
[23] Q. Zhao, H.J. Qi, T. Xie, Recent progress in shape memory polymer: New behavior, enabling materials, and mechanistic understanding, Prog. Polym. Sci. 49–50 (2015) 79–120, https://doi.org/10.1016/j.progpolymsci.2015.04.001.
[24] Y.L. Xia, Y. He, F.H. Zhang, Y.J. Liu, J.S. Leng, A Review of Shape Memory Polymers and Composites: Mechanisms, Materials, and Applications, Adv Mater 33 (6) (2021). https://doi.org/ARTN 200071310.1002/adma.202000713.
[25] S.J.A. Ali, D. Rahmatabadi, M. Baghani, M. Baniassadi, Experimental evaluation of mechanical properties, thermal analysis, morphology, printability, and shape memory performance of the novel 3D printed PETG-EVA blends, Macromol. Mater. Eng. 309 (10) (2024), https://doi.org/10.1002/mame.202400069.
[26] K. Mirasadi, D. Rahmatabadi, I. Ghasemi, M. Khodaei, M. Baniassadi, M. Bodaghi, M. Baghani, 3D and 4D Printing of PETG-ABS-Fe_3O_4 Nanocomposites with Supreme Remotely Driven Magneto-Thermal Shape-Memory Performance, Polymers-Basel 16(10) (2024). https://doi.org/ARTN 139810.3390/polym16101398.
[27] D. Rahmatabadi, A. Bayati, M. Khajepour, K. Mirasadi, I. Ghasemi, M. Baniassadi, K. Abrinia, M. Bodaghi, M. Baghani, Poly(ethylene terephthalate) glycol/carbon black composites for 4D printing, Mater Chem Phys 325 (2024). https://doi.org/ARTN 12973710.1016/j.matchemphys.2024.129737.
[28] D. Rahmatabadi, K. Mirasadi, A. Bayati, M. Khajepour, I. Ghasemi, M. Baniassadi, K. Abrinia, M. Bodaghi, M. Baghani, 4D printing thermo-magneto-responsive PETG-Fe_3O_4 nanocomposites with enhanced shape memory effects, Appl Mater Today 40 (2024). https://doi.org/ARTN 10236110.1016/j.apmt.2024.102361.
[29] X. Peng, Y. Han, G.A. Liu, J.Q. Li, B. Yi, G. Sa, S.F. Jiang, Effect of manufacturing process parameters on the compression and energy absorption properties of 4D-printed deformable honeycomb structure, Smart Mater Struct 33(7) (2024). https://doi.org/ARTN 07503510.1088/1361-665X/ad56e7.
[30] X.L. Zhou, L.Q. Ren, Z.Y. Song, G.W. Li, J.F. Zhang, B.Q. Li, Q. Wu, W.X. Li, L. Ren, Q.P. Liu, Advances in 3D/4D printing of mechanical metamaterials: From manufacturing to applications, Compos Part B-Eng 254 (2023). https://doi.org/ARTN 11058510.1016/j.compositesb.2023.110585.
[31] J.X. Qi, Z.H. Chen, P. Jiang, W.X. Hu, Y.H. Wang, Z. Zhao, X.F. Cao, S.S. Zhang, R. Tao, Y. Li, D.I. Fang, Recent Progress in Active Mechanical Metamaterials and Construction Principles, Adv Sci 9(1) (2022). https://doi.org/ARTN 210266210.1002/advs.202102662.
[32] T. van Manen, S. Janbaz, K.M.B. Jansen, A.A. Zadpoor, 4D printing of reconfigurable metamaterials and devices, Commun Mater 2(1) (2021). https://doi.org/ARTN 5610.1038/s43246-021-00165-8.
[33] R. Tao, L.T. Ji, Y. Li, Z.S. Wan, W.X. Hu, W.W. Wu, B.B. Liao, L.H. Ma, D.N. Fang, 4D printed origami metamaterials with tunable compression twist behavior and stress-strain curves, Compos Part B-Eng 201 (2020). https://doi.org/ARTN 10834410.1016/j.compositesb.2020.108344.
[34] X. Lin, F. Pan, K. Yang, J. Guan, B. Ding, Y.Z. Liu, K.J. Yang, B. Liu, Y.L. Chen, A Stair-Building Strategy for Tailoring Mechanical Behavior of Re-Customizable Metamaterials, Adv Funct Mater 31(37) (2021). https://doi.org/ARTN 210180810.1002/adfm.202101808.
[35] S.C. Han, M.C. Zou, X.X. Pu, Y.F. Lu, Y.C. Tian, H.J. Li, Y. Liu, F.Y. Wu, N.G. Huang, M.H. Shen, E.M. Song, D. Wang, Smart MXene-based bioelectronic devices as wearable health monitor for sensing human physiological signals, View-China 4 (4) (2023), https://doi.org/10.1002/Viw.20230005.
[36] J.L. Yang, L.M. Rong, W.X. Huang, Z.X. Wu, Q.L. Ding, H. Zhang, Y.Q. Lin, F. Li, C. W. Li, B.R. Yang, K. Tao, J. Wu, Flame-retardant, flexible, and breathable smart humidity sensing fabrics based on hydrogels for respiratory monitoring and non-contact sensing, View-China 4 (4) (2023), https://doi.org/10.1002/Viw.20220060.
[37] J.Z. He, J.J. Li, J.L. Zhang, P. Yi, X. Sun, G.Y. Han, X.F. Li, R.B. Zhang, X.F. Liu, R. H. Yu, Metal ions-assisted construction of SiO2/MXene/Fe3O4 aerogel as multifunctional electromagnetic wave absorbing material, Carbon 214 (2023). https://doi.org/ARTN 11826610.1016/j.carbon.2023.118266.
[38] L.Y. Liang, Q.M. Li, X. Yan, Y.Z. Feng, Y.M. Wang, H.B. Zhang, X.P. Zhou, C.T. Liu, C.Y. Shen, X.L. Xie, Multifunctional magnetic TiCT MXene/graphene aerogel with

superior electromagnetic wave absorption performance, ACS Nano 15 (4) (2021) 6622–6632, https://doi.org/10.1021/acsnano.0c09982.
[39] J.H. Wang, L. Zhang, J.F. Yan, J.N. Yun, W. Zhao, K. Dai, H. Wang, Y.S. Sun, MXene-based ultrathin electromagnetic wave absorber with hydrophobicity, anticorrosion, and quantitively classified electrical losses by intercalation growth nucleation engineering, Adv. Funct. Mater. (2024), https://doi.org/10.1002/adfm.202402419.
[40] F.S. Wu, P.Y. Hu, F.Y. Hu, Z.H. Tian, J.W. Tang, P.G. Zhang, L. Pan, M.W. Barsoum, L.Z. Cai, Z.M. Sun, Multifunctional MXene/C Aerogels for Enhanced Microwave Absorption and Thermal Insulation, Nano-Micro Lett 15(1) (2023). https://doi.org/ARTN 19410.1007/s40820-023-01158-7.
[41] N. Wu, Y.F. Yang, C.X. Wang, Q.L. Wu, F. Pan, R.A. Zhang, J.R. Liu, Z.H. Zeng, Ultrathin cellulose nanofiber assisted ambient-pressure-dried, ultralight, mechanically robust, multifunctional MXene aerogels, Adv. Mater. 35 (1) (2023), https://doi.org/10.1002/adma.202207969.